

Dynamic illumination of spatially restricted or large brain volumes via a single tapered optical fiber

Ferruccio Pisanello^{1,5} , Gil Mandelbaum^{2,5}, Marco Pisanello^{1,3}, Ian A Oldenburg², Leonardo Sileo¹, Jeffrey E Markowitz², Ralph E Peterson⁴, Andrea Della Patria¹, Trevor M Haynes², Mohamed S Emara^{1,3}, Barbara Spagnolo^{1,3}, Sandeep Robert Datta⁴, Massimo De Vittorio^{1,3} & Bernardo L Sabatini² 

Optogenetics promises precise spatiotemporal control of neural processes using light. However, the spatial extent of illumination within the brain is difficult to control and cannot be adjusted using standard fiber optics. We demonstrate that optical fibers with tapered tips can be used to illuminate either spatially restricted or large brain volumes. Remotely adjusting the light input angle to the fiber varies the light-emitting portion of the taper over several millimeters without movement of the implant. We use this mode to activate dorsal versus ventral striatum of individual mice and reveal different effects of each manipulation on motor behavior. Conversely, injecting light over the full numerical aperture of the fiber results in light emission from the entire taper surface, achieving broader and more efficient optogenetic activation of neurons, compared to standard flat-faced fiber stimulation. Thus, tapered fibers permit focal or broad illumination that can be precisely and dynamically matched to experimental needs.

Optogenetic modulation of neuronal activity has become the dominant method of examining the behavioral consequences of activity in specific neuronal populations *in vivo*. This is due to the synergy of advances in two distinct but well-connected fields: the development of ever-improving light-activated modulators of electrical activity^{1–3} and the development of technologies for delivering light within the brains of free-moving animals^{4–8}. Nevertheless, attaining the full potential of optical neural control requires new technologies to better control the spatial extent of light delivery and to more precisely match illumination to heterogeneous brain structures.

In certain applications, it is necessary to deliver uniform illumination to large brain areas, whereas for others confined illumination of small brain volumes is preferred. Ideally, both modes of illumination could be accomplished via a single, reconfigurable device. To this aim, several approaches have been developed, including multiple implanted waveguides^{8–10}, multiple microlight delivery devices (μ LEDs)^{6,7,11,12}, holographic illumination via head-mounted objectives¹³ and multipoint emitting optical fibers^{14,15}. However, these techniques have limitations: implanting multiple waveguides is highly

invasive, μ LEDs can heat tissue during prolonged illumination and multipoint emitting optical fibers require higher input laser power to produce viable optogenetic control. Likely due to the difficulty and cost of building the required devices, these approaches have not been broadly used in neuroscience labs. Indeed, the most common light delivery method for optogenetic experiments remains flat-faced optical fibers (FFs), which deliver highly spatially heterogeneous illumination to a relatively small and fixed brain volume near the fiber facet. Furthermore, due to the relatively large, flat area of the cleaved end, these fibers can cause substantial tissue damage during insertion.

Here we describe a tapered optical fiber (TF) whose emission properties can be simply and dynamically reconfigured to switch between relatively homogenous light delivery to a large volume and spatially restricted illumination. Multiple wavelengths of light can be independently modulated and directed to subvolumes of interest. The device consists of a single thin, sharp waveguide, thus minimizing invasiveness. To demonstrate the suitability of this approach for more uniform and efficient illumination of extended brain structures, experiments were performed in the primary motor cortex and striatum of awake head-restrained and freely moving mice. We demonstrate that by controlling the angle at which light is injected into the fiber, TFs can emit light from subportions of the taper to produce spatiotemporally resolved light patterns that subsample the volume of interest. We used this approach to achieve site specific optogenetic stimulation and demonstrate that activation of indirect pathway striatal projection neurons (iSPNs) in dorsal vs. ventral striatum has different effects on locomotion in mice exploring an open arena. Thus, TFs provide a simple, inexpensive and easy-to-operate multipurpose system for optical control of neural activity.

RESULTS

Design principles of tapered optical fibers

TFs are multimode fiber optics that have been engineered to taper gradually from their full width (125–225 μ m) to \sim 500 nm. The taper angle is small ($2^\circ < \Psi < 8^\circ$), such that the taper length varies between 1.5–5.6 mm (**Fig. 1**). This design was chosen to permit smooth insertion into the brain, reduce the implant cross-section and expose a

¹Istituto Italiano di Tecnologia (IIT), Center for Biomolecular Nanotechnologies, Arnesano, Lecce, Italy. ²Department of Neurobiology, Howard Hughes Medical Institute, Harvard Medical School, Boston, Massachusetts, USA. ³Dipartimento di Ingegneria dell'Innovazione, Università del Salento, Lecce, Italy. ⁴Department of Neurobiology, Harvard Medical School, Boston, Massachusetts, USA. ⁵These authors contributed equally to this work. Correspondence should be addressed to F.P. (ferruccio.pisanello@iit.it) or B.L.S. (bernardo_sabatini@hms.harvard.edu).

Received 22 December 2016; accepted 18 May 2017; published online 19 June 2017; doi:10.1038/nn.4591

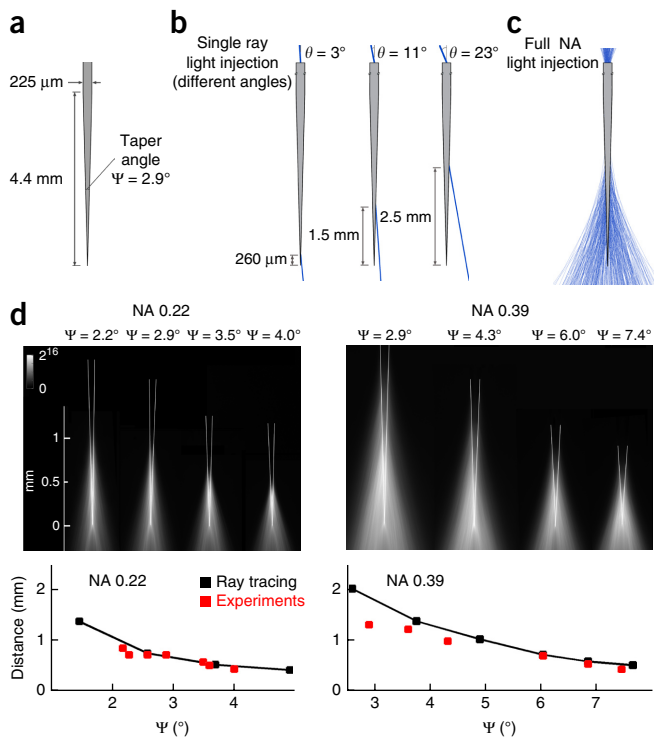


Figure 1 Emission properties of TFs. (a) Schematic representation of a typical TF geometry (NA = 0.39; taper angle, $\Psi = 2.9^\circ$; taper length, 4.4 mm; core and cladding diameters, 200 and 225 μm , respectively). (b) Ray-tracing simulations of emissions from the taper tip resulting from injecting a single ray into the fiber at different angles. (c) Ray distributions resulting from injecting light using the full NA of the fiber. (d) Top: fluorescence generated by light emitted from tapered fibers with the specified geometries immersed in a fluorescein solution. Bottom: calculated (black) and measured (red) emission lengths (evaluated as the full width at half maximum, $L_{0.5}$) for 0.22-NA (left) and 0.39-NA (right) TFs as a function of the taper angle. 0.22-NA TFs have core and cladding diameters of 50 and 125 μm , respectively, whereas 0.39-NA TFs have core and cladding diameters of 200 and 225 μm .

large area of the fiber for potential light emission. Ray-tracing and geometric models demonstrate the working principle of the device (Fig. 1a,b). A ray injected into the core of the fiber with an input angle θ is guided to the tapered region via total internal reflection. At each reflection of the ray, its propagation angle with respect to the fiber optical axis increases by an amount equal to the taper angle Ψ (Supplementary Fig. 1). This occurs until a critical section is met, at which total internal reflection is lost and the ray radiates into the surrounding medium. Increasing θ increases the distance between this light-emission point and the taper tip (Fig. 1b) in a manner determined by the fiber numerical aperture (NA) and taper angle (see Supplementary Fig. 2 for sample optical fibers with NA = 0.22 and NA = 0.39 and $\Psi = 2.2^\circ$ and $\Psi = 2.9^\circ$, respectively). Therefore, the light input angle θ selects the output zone along the length of a specific taper.

A consequence of the dependence of the position of light emission on θ is that TFs can be used to emit light along the fiber in two fundamentally different ways. First, when light is injected into the TF using its full NA, light is emitted from a broad extent of the taper (Fig. 1c), as desired for illumination of spatially extended brain regions, for example, the entire cortical thickness or the dorsal–ventral axis of the

striatum. For a fiber of a particular NA, the length of the light-emitting segment (L) depends mainly on the taper angle. Ray tracing simulations indicate that L can be tailored from a few hundred micrometers up to a few millimeters in the case of 0.22- and 0.39-NA fibers with taper angles Ψ ranging from 2.2° to 7.4° (Supplementary Fig. 3).

We experimentally verified this effect in 0.22- and 0.39-NA fibers by immersing TFs in a fluorescein solution and imaging the resulting fluorescence distribution (Supplementary Fig. 4). Decreasing the taper angle increases the length of the emitting segment to ~ 1 mm for 0.22-NA fibers with 50- μm core and 125- μm cladding (50/125- μm core/cladding) fibers and to ~ 2 mm for 0.39-NA fibers with 200/225- μm core/cladding (Fig. 1d). Thus, in this light-injection mode, a TF with the proper NA and taper angle can be chosen to match the linear extent of light output to the size of many mouse brain structures.

To compare the ray-tracing model with experimental results, we evaluated the emission length, referred to as $L_{0.5}$, over which the delivered intensity is more than 50% of its peak (Supplementary Fig. 4). We found good agreement between modeling and experiments for both 0.22- and 0.39-NA fibers (Fig. 1d and Supplementary Fig. 4). The differences observed at low Ψ for 0.39-NA fibers arise because the taper is assumed to be linear in the ray-tracing model, whereas the real structure has a modestly parabolic shape (Supplementary Fig. 5). The diameter at which light starts to outcouple and the total light power delivered are nearly independent of the taper angle (Supplementary Fig. 6). As a consequence, TFs with lower taper angles spread the available power over a larger taper surface (Supplementary Figs. 7 and 8), potentially allowing light delivery to elongated brain regions.

Illumination of large brain volumes with TFs

FFs are commonly inserted just above a brain volume of interest and the delivered light is strongly attenuated by the tissue, allowing excitation of neurons located only up to a few hundred micrometers from the fiber end^{16–18}. Significant excitation of more distant neurons requires large increases in laser power to overcome the approximately exponential decay in power density from the fiber face. In contrast, by virtue of their thin and sharp edge, TFs can be inserted into the volume of interest and light delivered along the length of the taper (Fig. 2). To evaluate the illumination pattern achieved in light-absorbing and scattering brain tissue, we implanted TFs and FFs into fluorescein-impregnated fixed mouse brain slices and imaged the fluorescence generated by light emitted from each fiber (Fig. 2a). As expected, FFs illuminate a small brain volume and fluorescence is strongly attenuated after a few hundred micrometers from the emitting flat-ended facet (Fig. 2b). In contrast, TFs emit light along the taper length, resulting in elongated and more homogenous illumination of the tissue (Fig. 2c,d).

The differences in tissue illumination achieved by TF and FF arise from two important features: (i) TFs emit light from a larger surface, i.e., the cone defined by L and Ψ ; and (ii) light emerges from the TFs at a nonzero angle with respect to the taper axis (Fig. 1c). As a consequence, tissue absorption and scattering do not determine light distribution along the fiber axis, as in FFs, but along the direction of emitted light, which has a significant component perpendicular to the taper axis. Notably, the depth of the excited volume can be tailored by selecting the fiber taper geometry and NA, instead of by increasing the laser power as commonly done in experiments with FFs. For instance, TFs with NA = 0.22 and $\Psi = 2.2^\circ$ illuminate the whole cortical depth, whereas TFs with NA = 0.39 and $\Psi = 2.9^\circ$ target most of the depth of the striatum (Fig. 2c,d).

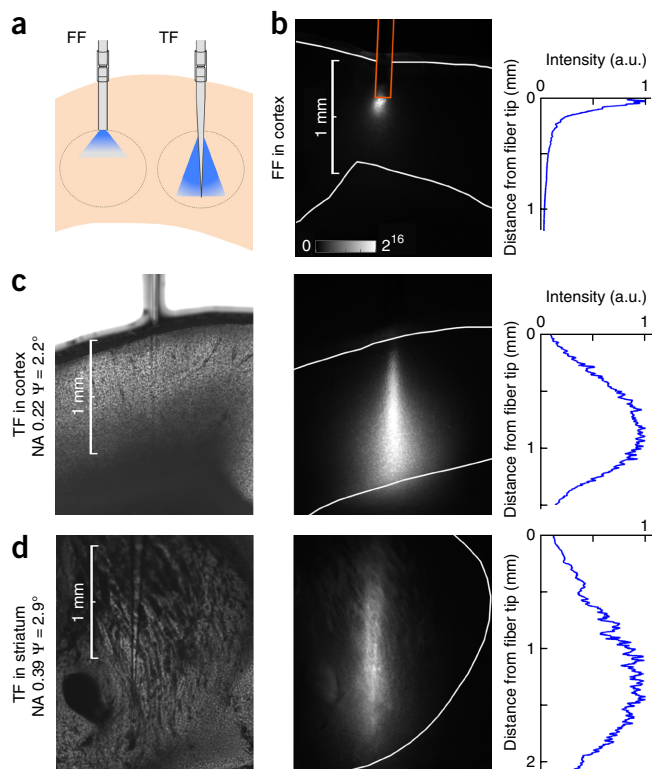


Figure 2 Emission properties of TFs in brain slices. **(a)** Schematic of light delivery in brain tissue through FFs and TFs. **(b)** Left: fluorescence induced by light emission from an FF implanted into cortex in a fluorescein-impregnated brain slice. Gray scale represents fluorescence intensity in arbitrary units of a linear scale. Right: normalized fluorescence intensity profile in the tissue starting from the fiber end face. **(c, d)** Brightfield images (left) identify the positions of the TFs in the fluorescein-impregnated cortical or striatal brain slice used for acquisition of the fluorescence images (middle). Gray scale is as in **b**. Right: normalized profiles of fluorescence intensities beside the taper, starting from the first emission point.

In vivo examination of effective excitation in striatum, a large brain structure

To characterize the efficacy of TFs for *in vivo* optogenetics, we compared the ability of TFs and FFs to activate channelrhodopsin-2 (ChR2)-expressing cells in striatum. Either a TF (NA = 0.39 and $\Psi = 2.9^\circ$) or an FF (NA = 0.22 or 0.39) was implanted in the striatum of adult transgenic mice (*Ador2a-Cre;Ai32*) expressing ChR2 in iSPNs (**Fig. 3**). This mouse line was selected for analysis because iSPNs are GABAergic neurons that locally inhibit other striatal neurons and inhibit recurrent excitatory inputs into striatum, minimizing secondary activation of cells not expressing ChR2 (ref. 19). The TF was implanted at a depth of 3.7 mm and the FF at 2.3 mm, respectively. Light (473 nm, 1 mW outputted at fiber exit) was delivered at a 30-s on, 30-s off cycle for 1 h to awake animals in their home cages. To compare the spatial distribution of cells activated by light delivered through TFs and FFs, animals were killed for analysis 2 h after stimulation, and we performed fluorescence immunohistochemistry for c-Fos, the protein product of an immediate early gene whose expression is regulated by neuronal activity²⁰. c-Fos was induced more uniformly across the ~2-mm dorsal–ventral extent of the striatum in TF-implanted animals compared to FF-implanted animals (**Fig. 3a–d**). Furthermore, although light delivery through the TF stimulated cells throughout the dorsal–ventral

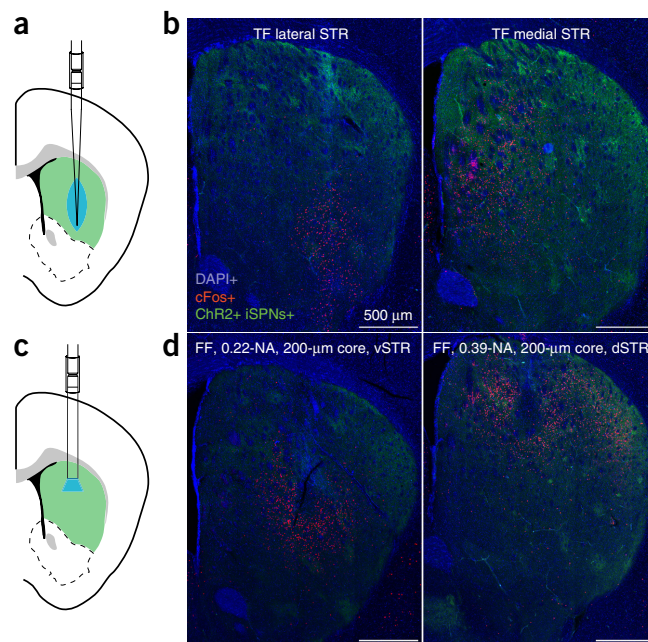


Figure 3 *In vivo* examination of effective excitation in striatum. **(a)** Schematic of experimental preparation, showing a TF inserted into the striatum (green) of a mouse expressing ChR2 in iSPNs and the area of illumination (blue shading). **(b)** c-Fos expression (red) in the striatum (coronal section, 0.85 mm anterior to bregma) of an animal expressing ChR2-YFP in iSPNs (green) after light stimulation delivered by a TF in lateral (left) or medial (right) striatum. DAPI is shown in blue. Representative image of two independent replicates. **(c)** Schematic of experimental preparation, as in **a**, showing placement of an FF. **(d)** As in **b**, showing c-Fos induction by light delivery from an FF in dorsal (left, 0.22-NA) or ventral (right, 0.39-NA) striatum. Representative image of two independent replicates. Scale bars, 500 μ m.

axis (i.e., along the axis of the fiber), differential placements of the fiber permitted selective stimulation of either lateral or medial sub-regions of striatum (**Fig. 3b**). Thus, as suggested by the simulations and fluorescence excitation *ex vivo* (**Figs. 1 and 2**), TFs deliver light *in vivo* across a spatially extended volume of tissue surrounding the thin fiber. Minimal c-Fos was induced in animals that expressed ChR2 in iSPNs but that were not stimulated and in wild type animals without ChR2 that did receive light stimulation (**Supplementary Fig. 9**). Lastly, a clear advantage of TFs, likely resulting from their submicron sized tips, was diminished tissue damage and activation of astrocytes and microglia compared to FFs (**Supplementary Fig. 10**).

Optogenetic control of motor cortex with TFs

To examine the potential benefits of more uniform light delivery *in vivo*, TFs were tested in the primary motor cortex of awake head-restrained *VGAT-ChR2-BAC* adult mice²¹, which express ChR2 in GABAergic neurons (**Fig. 4a**). A TF (NA = 0.22, $\Psi = \sim 2.2^\circ$) and FFs were implanted serially near a 16-contact silicon multielectrode array (Neuronexus). The FFs were placed such that the faces were at the same depth as the first emission point (shallow position) or the tip (deep position) of the TF. We delivered five 50-ms pulses of 473-nm light at 5 Hz, repeated every 3 s, 80 times. Output powers from the TF and FF were matched, to examine the efficiency of each fiber type to inhibit cortex via stimulation of GABAergic interneurons. TFs more effectively suppressed cortical activity at lower power levels (**Fig. 4b** and **Supplementary Fig. 11**): inhibition with TFs was obtained at

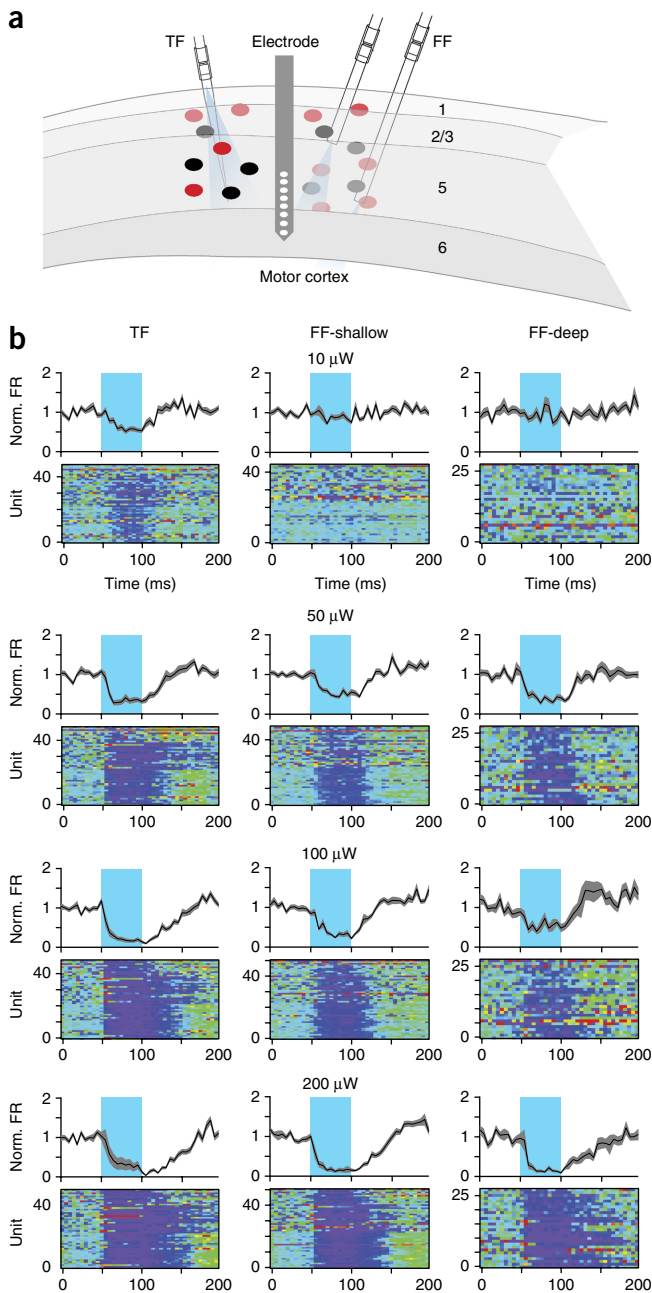


Figure 4 Optogenetic manipulation of motor cortex with TFs and FFs. (a) Schematic of the experimental preparation. A 16-channel multi-electrode array (gray; white circles indicate the contacts) was placed in primary motor cortex of a *VGAT-ChR2-BAC* transgenic mouse and maintained throughout the experiment. Units were recorded throughout cortical layers. A TF or FF was placed in cortex in either a shallow or a deep position. The firing rates of individual neurons (black and red ellipses) were compared during the basal period or during 50-ms optogenetic excitation of cortical GABAergic interneurons (red ellipses). (b) Top: average normalized firing rates (FR, black line; shaded area shows s.e.m.) across cells with and without light; cyan regions show light delivery (50-ms stimulation periods). Bottom: pseudocolored representations of normalized, across-trial average firing rates of each unit as a function of time. The color scale ('rainbow' in Igor Pro) indicates relative firing rates of each cell (0, dark blue, to 3, red) normalized to its baseline (0–50 ms). Data ($n = 45, 49, 51, 51, 28, 28, 28, 28, 48, 49, 49$ and 49 cells) are shown for each fiber configuration (left, TF; middle, FF-shallow; right, FF-deep) and at four power levels (10-, 50-, 100- and 200- μ W total emissions from each fiber before implantation in the brain).

$\sim 10 \mu\text{W}$ ($\sim 0.20 \text{ mW per mm}^2$; see **Supplementary Fig. 8** for estimated power density distribution along the taper) whereas FFs (NA = 0.22) required ~ 5 -fold higher power output to obtain a comparable effect at both depths ($50 \mu\text{W}$; $\sim 25 \text{ mW per mm}^2$; see the brain tissue light transmission calculator at <http://web.stanford.edu/group/dlab/optogenetics/>). Moreover, even at higher powers, inhibition was more pronounced with TFs, suggesting that tapered fibers stimulate a higher number of ChR2-expressing GABAergic neurons.

Dynamical selection of illuminated brain regions

A further benefit provided by TFs is the ability to dynamically control the illumination volume by changing the light entry angle θ at the input end of the fiber. The angle θ defines the subset of guided modes injected into the fiber^{14,15}, which in turn determines the cross-section of the taper at which light emits. The position of the emitting section along the taper depends on θ , as expected from the ray tracing simulations (**Supplementary Fig. 12** and **Supplementary Video 1**). In particular, with low input angles, light outcouples close to the taper tip, whereas light injected at high input angles is mainly emitted at sections farther from the tip.

To characterize the geometrical emission properties of TFs as a function of θ (**Fig. 5**), we implemented a simple optical path in which θ is changed by translating a mirror (**Supplementary Fig. 13a**). Monitoring the fluorescence generated by a TF inserted into a fluorescein solution showed that the emitting segment ($\sim 300 \mu\text{m}$ long) could be moved almost continuously along a segment of taper $\sim 1 \text{ mm}$ or $\sim 1.5 \text{ mm}$ long, respectively, in 0.22-NA, $\Psi = 2.2^\circ$ or 0.39-NA, $\Psi = 2.9^\circ$ TFs (**Fig. 5a,b**). Notably, total delivered light power was nearly independent of θ , except for input angles very close to the maximum acceptance angle (**Fig. 5c**). To rapidly scan the illumination across brain volumes, we used a launching system with a scanning galvanometer and relay optics to change θ (**Supplementary Fig. 13b**). This permitted rapid switching between different emission segments (**Supplementary Video 2**) and near continuous movement of the emitting segment along the taper (**Supplementary Video 3**). Several launching paths could be combined to outcouple multiple wavelengths at the same time from independently addressable emission segments (**Supplementary Fig. 13** and **Supplementary Video 4**).

To examine the suitability of this technique for restricted light delivery in brain tissue, site-selective light delivery as a function of θ was evaluated in fluorescein-stained acute mouse brain slices. Both 0.22-NA, $\Psi = 2.2^\circ$ and 0.39-NA, $\Psi = 2.9^\circ$ TFs allowed near-continuous tuning of the illuminated brain region in both cortex and striatum (**Fig. 5d–g**). Tissue absorption and scattering shortened the propagation of emitted light into the tissue, further constraining the spatial geometry of the illuminated area. This led to spatially separated light delivery volumes, resulting in an easy-to-use and versatile method to direct the light stimulus along a $\sim 2 \text{ mm}$ segment by implanting a single fixed fiber.

In vivo multisite stimulation

Selection of the emitting region of the taper is possible because different input angles generate different sets of guided modes in the fiber¹⁵ that outcouple at different taper sections. However, while propagating into the fiber, subsets of guided modes may undergo modal mixing induced by fiber impurities and bends. This could redistribute part of the guided light power to other modes and rearrange light emission along the taper. To evaluate the viability of using TFs for site-selective light delivery in moving mice, we measured the effects of bending and shaking on TF light output (**Supplementary Fig. 14**). For a fixed input angle ($\theta = 17^\circ$), the patch fiber carrying light to a TF with NA = 0.39

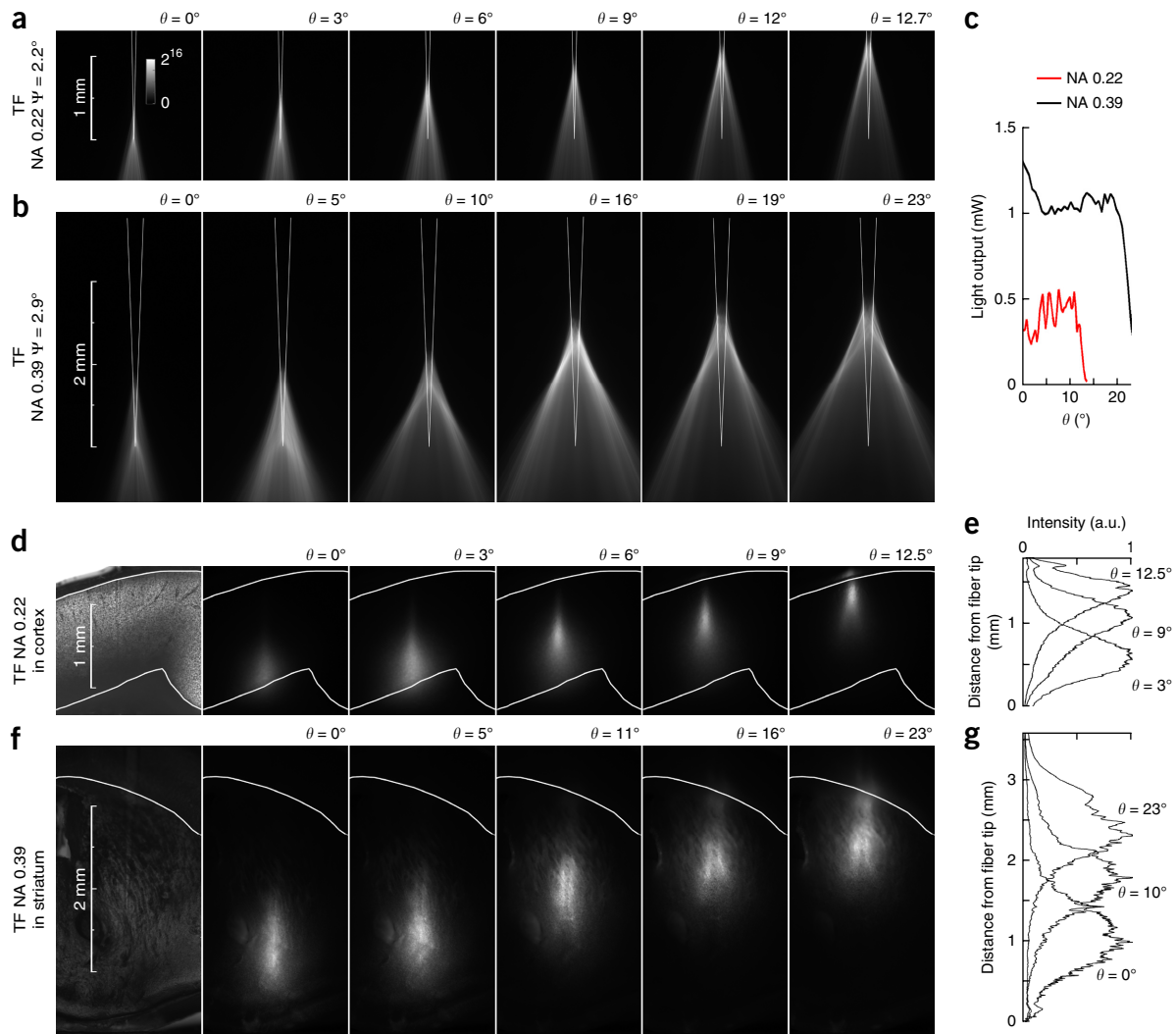


Figure 5 Site-selective light delivery with TFs. **(a)** Light delivery geometry for several values of light injection angle θ with a 0.22-NA, $\Psi = 2.2^\circ$ TF in a fluorescein solution. Gray scale represents fluorescence intensity in arbitrary units and is the same for all panels. **(b)** Light delivery geometry for several values of light injection angle θ with a 0.39-NA, $\Psi = 2.9^\circ$ TF in a fluorescein solution. **(c)** Total output power for a fixed input of 2.25 mW for a 0.22-NA, $\Psi = 2.2^\circ$ TF (red) and a 0.39-NA, $\Psi = 2.9^\circ$ TF (black). **(d)** Site-selective light delivery with a 0.22-NA, $\Psi = 2.2^\circ$ TF implanted into the cortical region of a fluorescent-stained mouse brain slice. **(e)** Normalized fluorescence intensity profiles, measured beside the taper, from the fluorescence images in **d**. **(f)** Site-selective light delivery with a 0.39-NA, $\Psi = 2.9^\circ$ TF implanted into the striatum of a fluorescent-stained mouse brain slice. **(g)** Normalized fluorescence intensity profiles, measured beside the taper, from the fluorescence images in **f**.

and $\Psi = 2.9^\circ$ was shaken and bent while emission into a fluorescein droplet was recorded at high frame rate (~100 frames per s (fps); **Supplementary Videos 5–7**). The fluctuations in fluorescence peak intensity, full-width-at-half-maximum and center were each less than 5% with fiber shaking and bending (**Supplementary Fig. 14**).

To demonstrate the feasibility of multisite optogenetic stimulation through a TF in an individual animal, TFs were designed (NA = 0.39, $\Psi = 2.3^\circ$) and implanted spanning the dorsal and ventral medial striatum of adult mice expressing ChR2 in iSPNs (*Ador2a-Cre;Ai32*). An optical pathway was designed (**Fig. 6a**) and calibrated to deliver a similar power density from the distal (ventral striatum) and proximal (dorsal striatum) sites (**Fig. 6c**) using, respectively, 8° (θ_1) and 22.5° (θ_2) launch angles (**Fig. 6a** and **Supplementary Fig. 15**).

Eight days after implant surgery, mouse spontaneous locomotion was monitored in an open circular arena with 3D time-of-flight cameras²². Light was delivered to the brain via an optical commutator, a

lightweight patch cord (200- μ m core, 0.39-NA, 1 m long) and two fiber–fiber junctions as typically used for unrestrained mouse behavior experiments (**Fig. 6a,b**). The experimental paradigm consisted of 3-min blocks of either no stimulation (NS) or laser input to the fiber at angle 1 (θ_1) or angle 2 (θ_2), repeated in the following pattern: NS– θ_1 –NS– θ_2 –NS– θ_1 –NS– θ_2 –NS, corresponding to alternating stimulation of ventral (θ_1) and dorsal (θ_2) striatum separated by periods of no stimulation (**Fig. 6c,d**). On the subsequent day, the order of ventral (θ_1) and dorsal (θ_2) stimulations were reversed, such that nine blocks per session were recorded in each of 2 d. Basic analyses of locomotion speed and orientation (**Fig. 6e**) reveal that stimulation at either dorsal or ventral striatum reduced locomotion and triggered contraversive spinning in individual mice (**Fig. 6f**), as expected for unilateral activation of iSPNs²³. Ventral stimulation via light injection at angle θ_1 inducing more profound effects (distance traversed in 3 min: NS: 3.16 ± 1.45 m, $n = 10$ 3-min blocks over 2 imaging

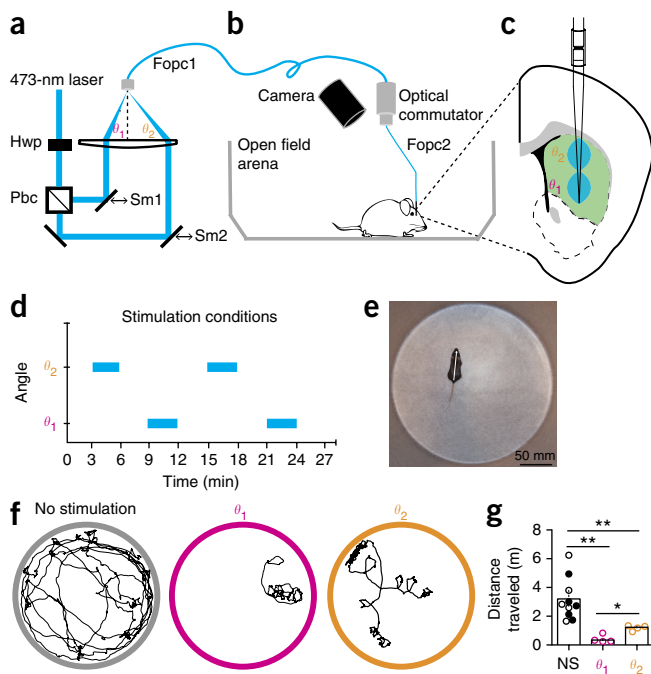


Figure 6 Selective light delivery with TFs in the open field. **(a)** Schematic of optical setup. The output of a polarized laser was passed through a $\frac{1}{2}$ -wave plate (hwp) to rotate the polarization before entering a polarizing beam cube (pbc), which transmits and reflects, respectively, horizontally and vertically polarized light. Rotation of the hwp determined the fraction of laser light entering each path. Each of the laser paths was directed to a 2-in (5.08-cm) collection lens via a sliding mirror (sm1 and sm2) that can be moved perpendicular to the optical axis of the lens to determine the launch angle into the first fiberoptic patch cable (fopc1). **(b)** Fopc1 was connected from the optical pathway shown in **a** to a commercial optical commutator, from which a second fiber optic patch cable (fopc2) led to the TF implanted in the animal. A depth camera above the arena monitored the mouse's location in 3D. **(c)** The TF was implanted in the striatum (0.85 mm anterior, 1.4 mm lateral and 4.1 mm dorsal of bregma) of a transgenic animal expressing ChR2-YFP in iSPNs to allow for stimulation of two regions of striatum. Light input at θ_1 (magenta) and θ_2 (orange) angles resulted in emissions targeting the ventral and dorsal striatum, respectively. **(d)** Example of stimulation experiment in the open field arena on day 1. Animals spent a total of 27 min in the open field, with 3-min sessions of light on at angle θ_1 or light on angle θ_2 alternating with 3-min periods of no light stimulation. On a subsequent day of analysis, the order of θ_1 and θ_2 stimulations were reversed. **(e)** Snapshot of a mouse in the open field, with an overlaid vector highlighting the simple feature extraction of position and orientation. **(f)** Example of the positions of one mouse during 3-min session of no stimulation (left), ventral stimulation (θ_1 , middle) and dorsal stimulation (θ_2 , right). **(g)** Quantification of distance traveled in the three conditions for the example mouse shown in **f**. Significant differences were observed between the no stimulation (NS, left), ventral stimulation (middle) and dorsal stimulation (right) conditions. Bars indicate the means of all data points from individual 3-min blocks, which are shown by circles (open circles, day 1; filled circles, day 2). $*P = 0.028$, $**P = 0.002$, using a two-tailed Mann-Whitney U test.

days for 1 mouse; ventral (θ_1): 0.41 ± 0.27 m, $n = 4$ blocks over 2 d for 1 mouse; dorsal (θ_2): 1.18 ± 0.18 m, $n = 4$ blocks over 2 d for 1 mouse; θ_1 versus θ_2 , $P = 0.0286$; θ_1 versus NS, $P = 0.002$; θ_2 versus NS, $P = 0.002$; **Fig. 6g**).

To understand whether dorsal versus ventral stimulation had qualitatively different behavioral consequences, mouse locomotion and posture (**Fig. 7a**) were analyzed using a machine-learning approach that automatically detects repeated time-varying 'syllables'

corresponding to the animal's postural dynamics²². This technique produces a hidden Markov model in which each state encapsulates the postural dynamics of the mouse in each expressed behavioral syllable. The model is built using 3D information derived from video collected at 30 Hz for all mice across all imaging sessions and stimulation conditions. In this case, 14 syllables were sufficient to explain ~94% of locomotion behavior in all sessions (NS, 87%; ventral (θ_1), 98%; dorsal (θ_2), 97%; **Fig. 7b**).

Consistent with the previously described effects of iSPN stimulation on locomotion²³ and those revealed by simple video tracking (**Fig. 6**), the most strongly induced behavior during stimulation was pausing (captured in syllables 1 and 2; percent of time spent in syllables 1 and 2: NS: 1%; ventral (θ_1): 74%; dorsal (θ_2): 38%), corresponding to a motionless mouse (**Fig. 7b** and **Supplementary Video 8**). The expression of these pause syllables varied across conditions and was most prominent during ventral stimulation (**Fig. 7b**).

Movement related syllables (syllables 3–14) were also differentially expressed across stimulation condition (percent of time spent in syllables 3–14: NS, 86%; ventral (θ_1), 24%; dorsal (θ_2), 59%; **Fig. 7b**). Furthermore, specific movement-related syllables were more strongly induced by dorsal stimulation (for example, syllables 4–6), whereas others showed the converse pattern (for example, syllables 3 and 7; **Fig. 7c**). Thus, these results are not consistent with ventral stimulation simply being more effective, as discrete motor actions were evoked by stimulation at each site. Each differentially modulated syllable represented a consistent but distinct motor action: syllable 6, more strongly evoked by dorsal stimulation, involved the animal shaking its body left and right, whereas syllable 7 was a spin to the left (head moved left while tail moved right; **Fig. 7d** and **Supplementary Videos 9** and **10**). Notably, the head and tail trajectories were similar during epochs of stimulation of the dorsal versus ventral striatum, despite their differences in expression frequency (**Fig. 7c,d**).

DISCUSSION

We demonstrate that TFs have several advantages for light delivery in the brain that might allow this tool to replace the flat-cleaved optical fibers that are typically used for optogenetic experiments. First, TFs are multipurpose, such that the same device allows either large-volume or site-selective light delivery. Second, by virtue of their tapered and smaller average cross section, TFs are minimally invasive and can be implanted directly into the brain region of interest. Third, they are simple to operate and compatible with optical equipment commonly present in neuroscience labs employing optogenetics.

Illumination of large brain volumes

When used to deliver light from the entire taper surface, TFs overcome one of the principal difficulties facing experiments in *in vivo* optogenetics: achieving uniform effective illumination of large brain structures with minimal invasiveness and light power. Although effective stimulation of neuron cell bodies expressing ChR2 can be obtained^{24,25} with power densities in the range 1–5 mW per mm² (and sometimes <1 mW per mm², depending on the sensitivity of the ChR2-expressing cells)²⁶, many published studies utilize orders of magnitude higher power^{16,27–29}. This likely arises because the FF is often positioned above the brain region of interest to minimize damage. Due to the exponential decrease in power density with distance from the FF, this necessitates the use of high light powers in order to stimulate cells throughout the nucleus^{16,17,30} and can result in local tissue heating by up to several degrees Centigrade¹⁸. By both permitting insertion of the fiber into the nucleus of interest and by delivering light along

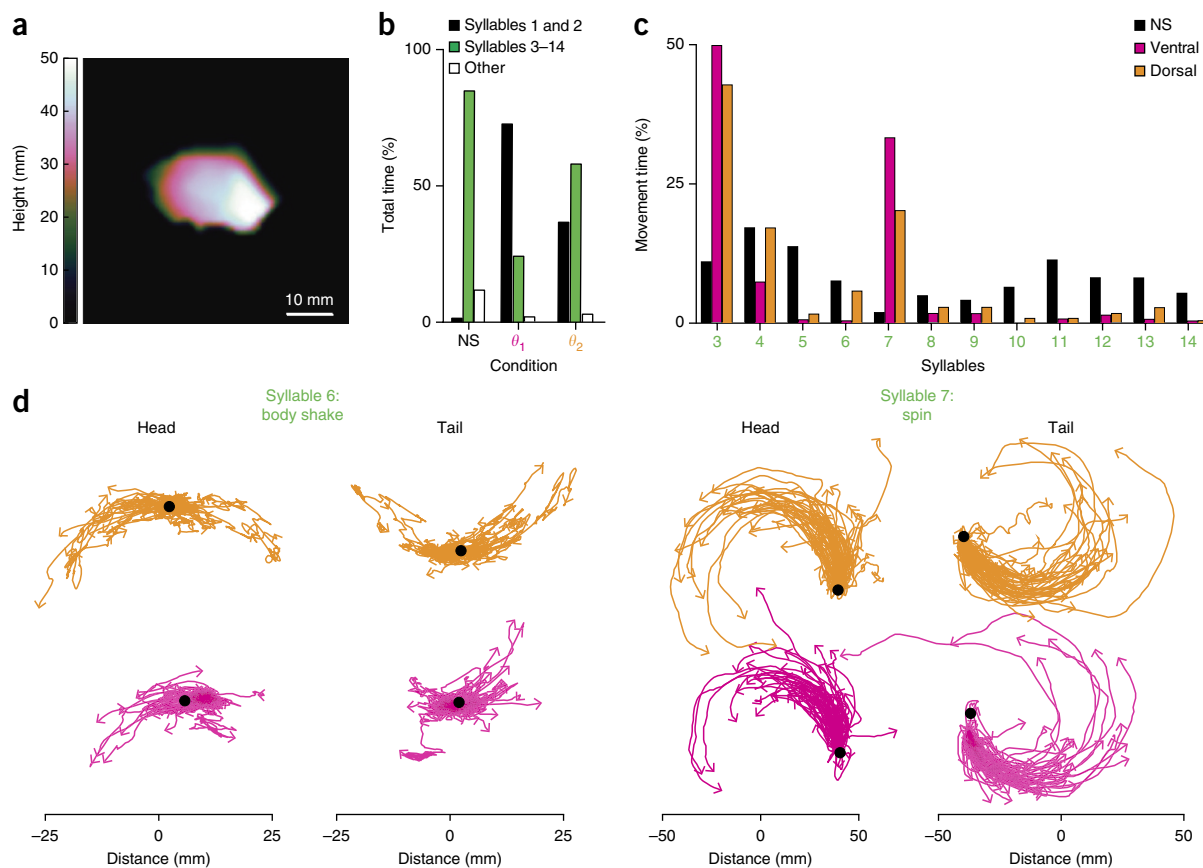


Figure 7 Mapping subsecond structure of behavior during optogenetic manipulation of ventral or dorsal striatum. (a) Snapshot of a mouse in the open field with the height of the body at each pixel indicated by the color scale. (b) The percent total behavior data (same mouse as in Fig. 6) categorized in each condition (NS, θ_1 and θ_2 stimulation) by the major pause-related syllables (1 and 2, black), the major movement-related syllables (3–14, green) and all other syllables (white). (c) Percent expression of the dominant nonpause, i.e., movement-related, syllables (3–14), showing differential expression of syllables across stimulation conditions. (d) The trajectories of the head and tail of the mouse relative to its body center for syllable 6 (left) and syllable 7 (right) in either the ventral (θ_1 , magenta) and dorsal (θ_2 , orange) stimulation conditions. Black dots depict the starting point of each of the aligned trajectories of the head and tail. Instances (limited to 100 randomly selected instances) of the trajectories of the head and tail relative to its body center are shown.

the linear extent of the taper, TFs achieve efficient light stimulation. This feature may be even more important when considering inhibitory and spectrally shifted opsins that may require more light to achieve effective neuronal perturbation.

Large brain area illumination with TFs is easily achieved with standard fiber-coupled lasers or light-emitting diodes (LEDs), including inexpensive LED-based commercial fiber launch systems (Supplementary Fig. 15) that naturally inject light over a large NA and produce emission over the fiber face. Furthermore, this approach is viable for chronic use in freely moving, tethered mice and for acute insertion in head-fixed mice.

Spatially restricted and dynamically controlled light delivery

TFs also permit rapidly adjusted delivery of light, even of multiple wavelengths, to subvolumes of brain tissue (Figs. 5–7 and Supplementary Videos 1–4). Site-selective light delivery is achieved using a simple optical setup that injects light into the fiber with a defined and adjustable angle, θ . At minimum, this setup consists of one lens and one translating mirror for slowly adjusting θ (Supplementary Fig. 13a). For high-speed control, three lenses and one galvanometric mirror (Supplementary Fig. 13b) can be used to change θ quickly. With this approach, the emitting region can be

modified step-by-step (every 20 ms in Supplementary Video 2) or continuously at various speeds (Supplementary Video 3).

Previous use of tapered fibers

Although the ability of TFs to provide uniform as well as dynamically controlled, restricted illumination has not been previously recognized, sharpened fibers have been sporadically used to increase light delivery angle, to reduce invasiveness and for biological discovery^{31–33}. This prior work exploits chemical etching of fibers³⁴, which can produce steep tapers of short lengths and has not been demonstrated to be capable of producing the long, gradual, tightly controlled tapers needed to illuminate large brain structures. In contrast, we pulled the fibers rapidly, after laser-heating, with very small taper angles, and we demonstrated reproducible fabrication of fibers with customized taper lengths and angles. Previous use of chemically etched fibers appears to have been intended to minimize tissue damage^{31,33} and provide a broader illumination angle from the tip³³. These studies may draw inspiration from previous work³² in which chemically etched fibers were attached to tetrodes to generate arrays of optrodes capable of both photostimulation and recording neural activity. In that study, light emission appears to be only from the taper tip and results in a broader illumination angle.

It is unclear in these studies if light was injected at the fiber back aperture using its full NA, as necessary to achieve light output from the entire fiber face. As far as we know, no previous study demonstrates, as we have done here, scanning output along the taper length (Fig. 5) or its application in freely moving animals (Figs. 6 and 7).

In addition, TFs can be coated with metal, with small openings to restrict light delivery. Lambelet *et al.* used TFs covered with aluminum to restrict light emission and collection to a ~100-nm fiber tip, as needed for near-field fluorescence³⁴. We previously restricted light emission from a fiber by coating it in gold and making small holes in the coating¹⁴. These metalized and milled fibers were hand-crafted, requiring hours of work by an individual at a highly specialized machine that combines focused ion beam milling within a scanning electron microscope and resulting in production costs of ~US\$1,000 per fiber. Furthermore, they could not be used for large volume illumination and provided only unidirectional illumination at fixed, predefined spots, whereas the new technology allows continuous and dynamic selection of illumination zones at a low cost.

Previously impossible classes of optogenetic experiment for biological discovery

From the perspective of an experimental neuroscientist, several classes of optogenetics experiments are enabled by exploiting the flexible and controllable nature of light delivery TFs provide. For example, subregions of the striatum subserve different functions, with specialized contributions to behavior evident along the dorsal–ventral as well as medial–lateral axes and coarse topographic mapping to cortex laid out along the anterior–posterior axis³⁵. We demonstrate (Figs. 3, 6 and 7) that with a TF it is possible to illuminate an elongated column of striatum that spans the dorsal–ventral axis and compare, in a single animal, the effects of selective optogenetic manipulation of subregions along the fiber axis. Given that the striatum spans several millimeters in the mouse, these experiments are impractical with standard FFs, as these can neither deliver light to the entire structure nor be repositioned for selective stimulation. Furthermore, with extended TFs, a single fiber can be inserted to deliver light to both cortex and striatum. Since light of different wavelengths can be outcoupled from different zones and independently controlled (Supplementary Video 4), TFs make it possible to examine the effects of interactions between areas. For example, one could examine whether the motor effects of motor cortex inhibition can be overcome by excitation of the striatum.

In addition, as optogenetics becomes accessible in primates³⁶, the larger brain structure will require the use of TFs for effective perturbations. For example, the visual cortex of macaque is several millimeters thick, with different cellular and receptive field properties in different layers³⁷. In the classic experimental system, current light delivery devices are unable to manipulate cells throughout all layers or, through a single device, test the effects of manipulations of superficial versus deep layer neurons. Furthermore, given the tight topographic organization of primate visual cortex and the use of individual animals for many recording sessions, it will be valuable to have a device such as a TF with gentle taper for multiple insertions in each recording session.

In summary, we exploited TFs with small taper angles to achieve near-uniform illumination of extended brain structures as well as to sample subregions of interest along a taper segment up to 2 mm long, while causing substantially less damage to the brain than use of FFs would. The devices were tested in both mouse motor cortex and striatum and showed that they required a ~5-fold lower excitation power threshold and excited a larger volume compared to flat-faced fibers.

Furthermore, we demonstrated their effective use through optical commutators and patch cords to compare the effects of stimulation of dorsal versus ventral striatum in individual unrestrained mice spontaneously exploring an arena. Coupled to the minimum invasiveness of the device, the simplicity of the technique and its intrinsic compatibility with both laser and LED sources, we suggest that this approach can greatly complement existing methods for light delivery in optogenetics experiments and has the potential to replace commonly used flat-faced fibers for many applications.

METHODS

Methods, including statements of data availability and any associated accession codes and references, are available in the [online version of the paper](#).

Note: Any Supplementary Information and Source Data files are available in the online version of the paper.

ACKNOWLEDGMENTS

F.P. acknowledges funding from the European Research Council under the European Union's Horizon 2020 research and innovation program (#677683); L.S., M.D.V. and B.L.S. are funded by the US National Institutes of Health (U01NS094190); and G.M., J.M., S.D. and B.L.S. are funded by the Simons Collaboration on the Global Brain. M.P. acknowledges funding from the Rotary Foundation and the Rotary International District 2120 (Global Grant GG1417647).

AUTHOR CONTRIBUTIONS

F.P., M.D.V., L.S. and B.L.S. conceived the TF technology; F.P., M.D.V., S.R.D. and B.L.S. supervised the research; F.P., G.M., M.P., I.A.O., L.S., J.E.M., R.E.P., A.D.P., T.M.H., M.S.E. and B.S. performed the research and analyses; F.P., G.M., and B.L.S. wrote the manuscript.

COMPETING FINANCIAL INTERESTS

The authors declare competing financial interests: details are available in the online version of the paper.

Reprints and permissions information is available online at <http://www.nature.com/reprints/index.html>. Publisher's note: Springer Nature remains neutral with regard to jurisdictional claims in published maps and institutional affiliations.

- Dawydow, A. *et al.* Channelrhodopsin-2-XXL, a powerful optogenetic tool for low-light applications. *Proc. Natl. Acad. Sci. USA* **111**, 13972–13977 (2014).
- Hochbaum, D.R. *et al.* All-optical electrophysiology in mammalian neurons using engineered microbial rhodopsins. *Nat. Methods* **11**, 825–833 (2014).
- Govorunova, E.G., Sineshchekov, O.A., Janz, R., Liu, X. & Spudich, J.L. NEUROSCIENCE. Natural light-gated anion channels: a family of microbial rhodopsins for advanced optogenetics. *Science* **349**, 647–650 (2015).
- Lee, J., Ozden, I., Song, Y.-K. & Nurmikko, A.V. Transparent intracortical microprobe array for simultaneous spatiotemporal optical stimulation and multichannel electrical recording. *Nat. Methods* **12**, 1157–1162 (2015).
- Canales, A. *et al.* Multifunctional fibers for simultaneous optical, electrical and chemical interrogation of neural circuits *in vivo*. *Nat. Biotechnol.* **33**, 277–284 (2015).
- Jeong, J.-W. *et al.* Wireless optofluidic systems for programmable *in vivo* pharmacology and optogenetics. *Cell* **162**, 662–674 (2015).
- Kim, T.I. *et al.* Injectable, cellular-scale optoelectronics with applications for wireless optogenetics. *Science* **340**, 211–216 (2013).
- Kwon, K.Y., Lee, H.-M., Ghovanloo, M., Weber, A. & Li, W. Design, fabrication, and packaging of an integrated, wirelessly-powered optrode array for optogenetics application. *Front. Syst. Neurosci.* **9**, 69 (2015).
- Zozos, A.N., Scholvin, J., Boyden, E.S. & Fonstad, C.G. Three-dimensional multiwaveguide probe array for light delivery to distributed brain circuits. *Opt. Lett.* **37**, 4841–4843 (2012).
- Schwaerzle, M., Elmlinger, P., Paul, O. & Ruther, P. in *Micro Electro Mechanical Systems (MEMS), 28th IEEE International Conference* 162–165 (2015).
- McAlinden, N., Gu, E., Dawson, M.D., Sakata, S. & Mathieson, K. Optogenetic activation of neocortical neurons *in vivo* with a sapphire-based micro-scale LED probe. *Front. Neural Circuits* **9**, 25 (2015).
- McCall, J.G. *et al.* Fabrication and application of flexible, multimodal light-emitting devices for wireless optogenetics. *Nat. Protoc.* **8**, 2413–2428 (2013).
- Szabo, V., Ventalon, C., De Sars, V., Bradley, J. & Emiliani, V. Spatially selective holographic photoactivation and functional fluorescence imaging in freely behaving mice with a fiberscope. *Neuron* **84**, 1157–1169 (2014).
- Pisanello, F. *et al.* Multipoint-emitting optical fibers for spatially addressable *in vivo* optogenetics. *Neuron* **82**, 1245–1254 (2014).

15. Pisanello, M. *et al.* Modal demultiplexing properties of tapered and nanostructured optical fibers for in vivo optogenetic control of neural activity. *Biomed. Opt. Express* **6**, 4014–4026 (2015).
16. Aravanis, A.M. *et al.* An optical neural interface: *in vivo* control of rodent motor cortex with integrated fiberoptic and optogenetic technology. *J. Neural Eng.* **4**, S143–S156 (2007).
17. Yizhar, O., Fenno, L.E., Davidson, T.J., Mogri, M. & Deisseroth, K. Optogenetics in neural systems. *Neuron* **71**, 9–34 (2011).
18. Stujenske, J.M., Spellman, T. & Gordon, J.A. Modeling the spatiotemporal dynamics of light and heat propagation for *in vivo* optogenetics. *Cell Reports* **12**, 525–534 (2015).
19. Oldenburg, I.A. & Sabatini, B.L. Antagonistic but not symmetric regulation of primary motor cortex by basal ganglia direct and indirect pathways. *Neuron* **86**, 1174–1181 (2015).
20. Greenberg, M.E., Ziff, E.B. & Greene, L.A. Stimulation of neuronal acetylcholine receptors induces rapid gene transcription. *Science* **234**, 80–83 (1986).
21. Zhao, S. *et al.* Cell type-specific channelrhodopsin-2 transgenic mice for optogenetic dissection of neural circuitry function. *Nat. Methods* **8**, 745–752 (2011).
22. Wiltschko, A.B. *et al.* Mapping sub-second structure in mouse behavior. *Neuron* **88**, 1121–1135 (2015).
23. Kravitz, A.V. *et al.* Regulation of parkinsonian motor behaviours by optogenetic control of basal ganglia circuitry. *Nature* **466**, 622–626 (2010).
24. Boyden, E.S., Zhang, F., Bamberg, E., Nagel, G. & Deisseroth, K. Millisecond-timescale, genetically targeted optical control of neural activity. *Nat. Neurosci.* **8**, 1263–1268 (2005).
25. Zhang, F. *et al.* Multimodal fast optical interrogation of neural circuitry. *Nature* **446**, 633–639 (2007).
26. Klapoetke, N.C. *et al.* Independent optical excitation of distinct neural populations. *Nat. Methods* **11**, 338–346 (2014).
27. Cardin, J.A. *et al.* Targeted optogenetic stimulation and recording of neurons *in vivo* using cell-type-specific expression of Channelrhodopsin-2. *Nat. Protoc.* **5**, 247–254 (2010).
28. Warden, M.R., Cardin, J.A. & Deisseroth, K. Optical neural interfaces. *Annu. Rev. Biomed. Eng.* **16**, 103–129 (2014).
29. Eshel, N. *et al.* Arithmetic and local circuitry underlying dopamine prediction errors. *Nature* **525**, 243–246 (2015).
30. Al-Juboori, S.I. *et al.* Light scattering properties vary across different regions of the adult mouse brain. *PLoS One* **8**, e67626 (2013).
31. Hanks, T.D. *et al.* Distinct relationships of parietal and prefrontal cortices to evidence accumulation. *Nature* **520**, 220–223 (2015).
32. Stark, E., Koos, T. & Buzsáki, G. Diode probes for spatiotemporal optical control of multiple neurons in freely moving animals. *J. Neurophysiol.* **108**, 349–363 (2012).
33. Gilmartin, M.R., Miyawaki, H., Helmstetter, F.J. & Diba, K. Prefrontal activity links nonoverlapping events in memory. *J. Neurosci.* **33**, 10910–10914 (2013).
34. Lambelet, P., Sayah, A., Pfeffer, M., Philipona, C. & Marquis-Weible, F. Chemically etched fiber tips for near-field optical microscopy: a process for smoother tips. *Appl. Opt.* **37**, 7289–7292 (1998).
35. McGeorge, A.J. & Faull, R.L. The organization of the projection from the cerebral cortex to the striatum in the rat. *Neuroscience* **29**, 503–537 (1989).
36. Afraz, A., Boyden, E.S. & DiCarlo, J.J. Optogenetic and pharmacological suppression of spatial clusters of face neurons reveal their causal role in face gender discrimination. *Proc. Natl. Acad. Sci. USA* **112**, 6730–6735 (2015).
37. Lund, J.S. & Boothe, R.G. Interlaminar connections and pyramidal neuron organisation in the visual cortex, area 17, of the Macaque monkey. *J. Comp. Neurol.* **159**, 305–334 (1975).

ONLINE METHODS

Animals. All mouse handling and manipulations were performed in accordance with protocols approved by the Harvard Standing Committee on Animal Care, following guidelines described in the US National Institutes of Health *Guide for the Care and Use of Laboratory Animals*. In this study, we used both male and female mice (age > P60). We used the *VGAT-ChR2* mouse from the Jackson Laboratory (B6.Cg-Tg(Slc32a1 COP4*H134R/EYFP) 8Gfng/J, stock #014548) and the *Adora2a-Cre* mouse line from GENSAT: (B6.FVB(Cg)-Tg (Adora2acre) KG139Gsat/Mmucd) crossed with the *Ai32* mouse line from Jackson Laboratory (RCL1-ChR2(H134R)/EYFP, stock #012569). In addition, we used C57BL mice from Charles River (C57BL/6NCRl, stock #027).

Ray-tracing simulations. We used commercial optical ray-tracing software Zemax-OpticStudio (<http://www.zemax.com/>) to design and simulate the performances of TFs. The single TF was modeled as a straight core/cladding segment followed by a conical taper. The materials forming all the components of the TFs and the surrounding media were assumed to be homogenous (refractive index constant in space). The core/cladding diameters were 50/125 μm and 200/225 μm for fibers with numerical apertures NA = 0.22 and NA = 0.39, respectively. Core/cladding refractive indexes were set as specified by the fiber producer: 1.464/1.447 for NA = 0.22 and 1.464/1.411 for NA = 0.39. Since the tapers were obtained by heating and pulling, commonly resulting in a melting of core and cladding materials in the tapered regions, the taper refractive index was assumed to be the average of core and cladding refractive indexes, weighted by the respective cross sectional areas of core and cladding. This resulted in taper refractive indexes of 1.450 for fibers with NA = 0.22 and 1.453 for fibers with NA = 0.39. The length of the core/cladding block was set to 4 mm, whereas the length of the taper was a function of the taper angle.

For results of simulations reported in **Figure 1b** and **Supplementary Figure 2**, the source was modeled as a single ray injected into the fiber, with a defined angle of incidence with respect to the fiber optical axis. For simulations reported in **Figure 1** and **Supplementary Figures 3** and **4**, a monochromatic source ($\lambda = 473 \text{ nm}$) was modeled as a bundle of unpolarized parallel rays with a Gaussian intensity profile. The source was focused into the core/cladding section of the fiber through a Zemax model of the experimentally used aspheric condenser (Rochester Precision Optics; <http://www.rpoptics.com/>). We used model A-375-A, with focal length $f = 7.49 \text{ mm}$, NA = 0.29 and clear aperture of 4.50 mm, for TFs with NA = 0.22 (input Gaussian beam radius = 1.66 mm, measured at $1/e^2$, resulting in a focused waist of 1.6 μm RMS spot radius), and used model A-390-A, with $f = 4.60 \text{ mm}$, NA = 0.47 and clear aperture of 4.90 mm, for fibers with NA = 0.39 (input Gaussian beam radius = 1.84 mm, measured at $1/e^2$, resulting in a focused spot of 1.9 μm RMS spot radius). The former coupler was used only with the NA = 0.22 optical fiber, with a Gaussian beam radius of 1.66 mm focused on the fiber core (with a 1.6- μm RMS spot radius); the latter was used with both fibers, with a Gaussian beam radius of 1.84 mm, producing a 1.9- μm RMS spot radius. For simulations displayed in **Supplementary Figure 12**, a parallel and unpolarized Gaussian beam with radius 25 μm at $1/e^2$ intensity was injected at different input angles.

The irradiance profile of the light outcoupled from the taper was recorded through a rectangular, pixelated detector laid along the taper sidewall (**Supplementary Fig. 4**). The detector length was set as the taper side length and its width was set to 20 μm . These profiles were then averaged along the short side of the detector and fitted with a Gaussian function. The full-width-at-half-maximum criterion was used to retrieve the emission length ($L_{0.5}$, measured axially from the taper tip) from the irradiance profiles. For each single ray tracing session, 5 million rays were launched into the system, and each ray was split at the boundary between two different media, according to Fresnel coefficients.

Ray tracing is appropriate for the modeling shown in **Figure 1** and **Supplementary Figures 2–4**. Mode theory (the Helmholtz equation³⁸) is typically employed for an accurate analysis of light propagation when the waveguide size is comparable to the wavelength of light. However, in our tapered fibers, this condition applies only close to the fiber tip. We describe the working principles of TFs using ray optics because the main effects we exploit take place not at the tip but rather over the whole extent of the tapered fiber, and they mostly occur at fiber diameters well above a few micrometers. Ray-tracing is used to characterize the full-NA injection method, with good agreement with experimental results (**Fig. 1d**). In the section “*In vivo* multisite stimulation” we describe the working principles of the device, based on selective modal outcoupling along the taper.

TFs stub preparation and optical measurements. Tapered optical fibers with taper angles in the range $2^\circ < \Psi < 8^\circ$ were obtained from Optogenix (<http://www.optogenix.com/>) and connected to a ceramic ferrules following the procedure described previously³⁹. A ceramic ferrule-SMA patch cable was used to connect the fiber stub to the optical setup displayed in **Supplementary Figure 4** for full-NA light injection or to the setups schematized in **Supplementary Figure 13** for site-selective light delivery. The taper was immersed in a fluorescent PBS:fluorescein solution or inserted in stained brain slices positioned under a 5 \times objective of a fluorescence Zeiss microscope equipped with a FITC filter. Images were acquired with a Hamamatsu Orca Flash 4.0. sCMOS camera at a resolution of 2,048 \times 2,048 pixels (pixel depth: 16 bit). Optical output power was measured in air. In the multi-wavelength experiment reported in **Supplementary Video 4**, the taper was immersed in a drop of diluted milk to induce scattering of outcoupled light and detected with a color CCD camera.

For imaging light delivery geometry in fixed brain slices, slices 200–400 μm thick were permeabilized with 0.1% Triton X-100 for 10 min to allow homogenous cell staining through the whole-brain slice thickness and then washed with 1 \times PBS three times. Slices were then incubated with Sybr Green 1:10,000 (Thermo Fischer Scientific Inc.) for 20 min on an orbital shaker in the dark and thoroughly washed with 1 \times PBS.

Analysis of c-Fos induction. Transgenic adult (*Adora2a-Cre;Ai32*) animals (age > P60) were anesthetized with isoflurane and placed in a small animal stereotaxic frame (David Kopf instruments). Under aseptic conditions, the skull was exposed and a small hole was drilled. Animals received 0.01 mg/g of sterile Ketofen (Zoetis). For FF-implanted animals and animal implanted with a TF in the lateral striatum, the hole was made 0.85 mm anterior and 1.95 mm lateral from bregma. For animals implanted with a TF in the medial striatum, the hole was made 0.85 mm anterior and 1.65 mm lateral from bregma. A TF (3.7 mm from pia) or FF (2.3 mm from pia) was inserted manually using a cannula holder (David Kopf instruments). The TF or FF was then glued in place (454 instant adhesive, Loctite), and the skull was covered with dental cement (CandB Metabond, Parkell Inc.). Regardless of the implant-surgery time, animals were kept under isoflurane anesthesia for a total of 1 h before stimulation started. Stimulation was delivered in 30-s on/off cycles for a total of 1 h (473-nm light, 1 mW outputted at fiber exit). Two hours after stimulation, animals were euthanized with 0.2 ml of 10% Fatal Plus solution (Vortech Pharmaceuticals) in saline before being perfused with 4% paraformaldehyde (PFA) in 0.1 M sodium phosphate buffer (PBS). Brains were postfixed for 24 h in PFA, washed in PBS and sectioned (50 μm) coronally.

Immunohistochemistry conditions were the same for all animals. In short, slices were incubated in PBS blocking solution containing 0.3% Triton X-100 (PBST) for 1 h at RT (20–22 $^\circ\text{C}$). Slices were then incubated over night at 4 $^\circ\text{C}$ in the same blocking solution with 1% goat serum and 1 $\mu\text{g}/\text{mL}$ c-Fos rabbit polyclonal IgG antibody (H-125, Santa Cruz Biotechnology). The next day, slices were rinsed 3 \times 10 min in PBS before being incubated in the blocking solution with secondary antibody (1 mg/mL goat anti-rabbit Alexa Fluor 647 or Alexa Fluor 594; Life Technologies). The slices were then rinsed again and mounted. After drying, slices were coverslipped with ProLong antifade mounting media containing DAPI (Molecular Probes) and imaged with an Olympus VS 120 slide-scanning microscope using a 10 \times objective.

Analysis of glial response to fiber insertion. The implant surgery was similar to the one described in the “Analysis of c-Fos induction” section, but both implants were positioned 0.8 mm anterior and 2.0 mm lateral to bregma. In addition, the TF was implanted at a depth of 4.0 mm and the FF at 3.5 mm. Adult (*C57BL/6NCRl*) animals (age > P60) were killed for analysis 48 h after surgery and as described above. To compare the spatial distribution of microglia and astrocytes activated near the implant, we performed fluorescence immunohistochemistry (as described above in the “Analysis of c-Fos induction” section) for GFAP (primary: rabbit anti-GFAP, Dako Z0334, 1:1,000 dilution; secondary: 1:1,000 goat anti-rabbit Alexa Fluor 555) and CD68 (primary: rat anti-CD68, Biorad MCA1957; 1:200 dilution; secondary: 1:1,000 goat anti-rat Alexa Fluor 647), respectively. Six coronal sections surrounding the implant were imaged with a VS120 Olympus slide-scanning microscope. Quantification of fluorescence intensity was performed in ImageJ (NIH). ROIs of striatum were determined based on the *Allen Brain Atlas* (2004). For each section, the total fluorescence intensity summed from the left and right hemispheres was normalized to 1, such

that the fluorescence per hemisphere was expressed as a fraction of the total for that section. No comparisons were made between sections.

Multielectrode array recordings. Recordings in primary motor cortex of adult (*VGAT-ChR2*) animals (age > P60) and offline analysis of spiking rates were accomplished as previously described¹⁹. Mice were habituated to head-restraint before the recording session. Only one fiberoptic (TF or FF) was inserted at a time and the effects of transient stimulation of cortical inhibitory neurons on identified units were examined. For each unit, spiking rates were normalized to the preillumination rate. Averages were calculated across neurons.

Open field surgery. The surgery for TF implant was as described above in the “Analysis of c-Fos induction” section, with coordinates for the TF in striatum being 0.85 mm anterior, 1.4 mm lateral and 4.1 mm dorsal of bregma. Adult (*Ador2a-Cre;Ai32*) animals (age > P60) recovered for 5 d after surgery and were handled for 3 d before experimentation.

Behavior. On the day of the experiment, animals were placed in the open field arena. The experimental model consisted of 3-min blocks of either no stimulation (NS), laser input to the fiber at angle 1 (θ_1) or laser input at angle 2 (θ_2), repeated in the following pattern: NS- θ_1 -NS- θ_2 -NS- θ_1 -NS- θ_2 -NS, alternating stimulation of ventral (θ_1) and dorsal (θ_2) striatum separated by periods of no stimulation. On the subsequent day of analysis, the order of ventral (θ_1) and dorsal (θ_2) stimulations were reversed.

Open field analysis. Mice were recorded using a Microsoft Kinect (v1), which records 3D video data at 30 frames per second. For data in **Figure 6**, scalar features were extracted using previously published methods²². For modeling data presented in **Figure 7**, the open field behavior was analyzed using previously published methods²². In brief, the data were subjected to machine-learning methods that describe the mouse's behavior as reusable subsecond modules, or syllables. All free parameters were set to the values described in Wiltschko *et al.*²² with the exception of the stickiness parameter, kappa, which sets the model's tendency to remain in the same syllable over time (rather than switch between different

syllables). This parameter is tuned so that the overall syllable duration distribution qualitatively matched a model-free analysis of behavioral change-points, as in Wiltschko *et al.*²². For this analysis we set kappa to 291,600. For positioning of the mouse in **Figure 7**, the head and tail position were computed first by fitting an ellipse to the image of the mouse. The head and tail positions were defined as the two points of the ellipse most distant from each other (i.e., the points of the ellipse that intersect with its principal axis).

Statistics. Statistical comparisons were performed in Prism (Graphpad) using nonparametric tests. For the data in **Figure 6**, a two-tailed Mann-Whitney *U* test was performed with $n = 10, 4$ and 4 for NS, θ_1 stimulation and θ_2 stimulation, respectively. For further details, see the main text and **Figure 6** legend. Each n value represents one 3-min imaging session, with half the sessions collected on day one and half on day 2. For the data in **Supplementary Figure 11**, a Kruskal Wallis ANOVA with Dunn's multiple-comparison correction was performed using $n = 45, 49, 51, 51, 28, 28, 28, 28, 48, 49, 49$ and 49 cells for 10-, 50-, 100- and 200- μ W power for the TF, shallow FF and deep FF. See the **Supplementary Figure 11** legend for further details. See the **Supplementary Methods Checklist** for further details. No statistical methods were used to determine sample sizes a priori. The sample size was chosen based on prior experience with similar experiments. Normality was not assumed and no per-sample calculation of variance was performed. No randomization or blind analysis was used. However, for **Figures 6** and **7** analysis was performed with automated routines with no user intervention and the stimuli were delivered in interleaved and counterbalanced orders. No criteria for data exclusion were used.

Data and code availability. All data and code are available from the authors upon reasonable request.

38. Saleh, B.E.A. & Teich, M.C. *Fundamentals of Photonics* 2nd edn. (Wiley Interscience, 2007).
39. Sparta, D.R. *et al.* Construction of implantable optical fibers for long-term optogenetic manipulation of neural circuits. *Nat. Protoc.* **7**, 12–23 (2011).